

CARMA Memorandum Series #42

**Exploring Power Patterns of Parabolic Antennas:
Implications for Water Vapor Radiometers**

Y.-S. Jerry Shiao, Leslie W. Looney and Edmund C. Sutton

University of Illinois at Urbana-Champaign

February 20, 2008

ABSTRACT

Water vapor radiometers (WVRs) are designed to compensate atmospheric phase fluctuations at millimeter and submillimeter wavelengths for radio interferometers on short time-scales. Water vapor clouds have been considered the major components that affect the phase fluctuation. Monitoring water vapor along the lines of sight of antennas and deriving path delay differences for each baseline should allow us to implement a phase correction scheme. However, ground-based antennas are surrounded by water vapor at various heights. The mechanism for detecting the water vapor columns of the antennas may be very different from the astronomical sources. To quantify the impact of the water vapor location on the WVR phase correction scheme, we explore the power patterns of antennas with a series of numerical simulations. In this memo, we define the water vapor detection efficiency as antenna temperature to water vapor brightness temperature ratio. With the simulations, we demonstrate that the detection efficiency substantially depends on the sizes and the heights of water vapor clouds. We suggest that this effect may play a key role in the WVR phase correction scheme and explain that the well-known scale factor of the 22 GHz water line varies in many WVR experiments.

1. Introduction

Astronomers constantly push the technical limits of telescopes to obtain the best observation for their scientific goals. For ground-based telescopes, one of the major limits is the atmosphere. An unstable atmospheric condition can seriously downgrade observational quality. To date, for radio interferometers, we monitor phase calibrators alternately during observations to correct phase fluctuations to achieve phase correction. However, monitoring phase calibrators sacrifices precious observational time and recovers the phase fluctuations only on long time-scales, tens of minutes to a half hour. Nearly one fourth of the time is devoted to phase calibration. Thus, we need a better phase correction scheme to improve observational efficiency.

Water vapor clouds have been known to cause the phase fluctuations in the millimeter to sub-millimeter regions (Waters 1976). Water vapor affects the refraction index of the atmosphere and produces different path delays for antennas. By monitoring the water vapor in the atmosphere, water vapor radiometers (WVRs) may provide sufficient information for deriving the path delays on short time-scales, a few seconds to minutes. Based on this premise, WVR systems, including 22 GHz (e.g. Marvel et al. 1998) and 183 GHz (e.g. Hills et al. 2000) receivers, have been build and tested by many radio astronomy associations. However, these projects seem to encounter unknown difficulties and only occasionally show correlations between the water vapor data and observed path delays (Chandler et al. 1998).

The path delays are varied by the water vapor clouds in the columns along the lines of sight of antennas to astronomical sources. The water vapor columns are very different sources from those of astronomy. They are in both the near- and far-field regions of the antennas unlike astronomical sources are only in the far-field. Indeed, water vapor is predominantly at the ground, which is in the near-field (Waters, 1976). The water vapor in the columns consist of various size water vapor clouds, which may fail to fully cover the antenna beams. Thus, the antenna temperatures and the brightness temperatures of the water vapor clouds are no longer equivalent. Without the information about the sizes and the heights of the clouds, the difference between these two temperatures may cause a problem in deriving the path delays. Moreover, the antenna temperature may depend on both the water vapor clouds inside and outside the antenna column.

To carefully examine the relationship between the antenna temperature and the brightness temperature, we have conducted numerical simulations to address this problem quantitatively. In this memo, first, we introduce the derivation of the path delay. Then, we show our simulation setup and results. Finally, we discuss and conclude the impact of finite-size water vapor clouds.

1.1. Atmospheric Model

The atmosphere can be modeled as a multi-layered structure, i.e. atmospheric parameters, like temperature, pressure and density, are functions of height. One can easily obtain the brightness

temperature of the atmosphere with atmospheric modeling programs, like the ATM code (e.g. Staguhn et al. 1998). Given ground temperature, pressure, and density and assuming that they are exponential functions of height, the atmospheric brightness temperature is

$$T_a = \int_0^\infty T_b(h)dh = \int_0^\infty T(h)(1 - e^{-\tau(h)}) \times e^{-\tau'(h)} dh, \quad (1)$$

where $T_b(h)$ is the brightness temperature and $T(h)$ is the corresponding temperature at h . T_a is the antenna temperature, which is the WVR output data. τ and τ' are the opacity of the layer at h and the total opacity from the ground to h , respectively.

Based on the ATM simulation, with 5 mm precipitable water vapor (pwv), the brightness temperature of the 22 GHz water vapor line is about 10 K. The scale factor that translates the brightness temperature to the corresponding path delay is 5 mm/K in approximation (Staguhn et al. 1998). To recover a path delay of 100 μm , the sensitivity of a 22 GHz WVR needs to be 3 mK, which is 0.3% of the 10 K. As a result, the deviation of the antenna temperature from the brightness temperature must be smaller than 0.3%, which is still a challenge to modern receivers.

1.2. Water Vapor Clouds

In the ATM simulation, the water vapor clouds are considered as infinite-size layers. The antenna temperature and the brightness temperature of the clouds are equivalent. However, in practice, the clouds are finite-size and the antenna temperature is different from the brightness temperature. Given the sensitivity requirement of the 22 GHz WVRs, we need to consider the impact of the finite-size clouds on the WVR phase correction scheme.

1.3. Near-field and Far-field

It is inevitable for ground-based antennas to 'see' water vapor, because of the atmosphere, an extended source that is even inside antenna horns that are without vacuuming (Thompson et al. 2001). The antenna field can be divided into three different regions, the far-field, the near-field and the reactive near-field regions as shown in Figure 1 (Balanis 1996). Since most water vapor is in the near-field and reactive near-field regions, the near-field and the reactive near-field water vapor are more critical to WVRs. However, in this memo, we ignore the effect of the reactive near-field, which likely contributes less than the others. The amount of the water vapor in this region is relatively small.

Gaussian beam analysis is a well-known mathematical tool to analyze near-field problems in the first order. However, to better quantify the impact of the finite-size water vapor clouds, we decide to numerically simulate the reception of an antenna in a two-dimensional space. Thus, we can

calculate the deviation of the water vapor detection precisely and illustrate the antenna patterns better.

2. Simulation Setup

Our strategy is to simulate a two-dimensionally parabolic antenna receiving radiation power emitted by finite-size sources. By sampling the sources at different positions on a plane, we can generate antenna power patterns as well. Three-dimensional simulations may best reflect reality but require extensive computing time and complex water vapor cloud models. Additionally, we replace the parabolic antenna with a linear antenna array in our code. Each antenna represents a small segment of a parabolic antenna. The antenna array is set up along the x -axis while the finite-size sources are in the first and second quadrants in Figure 2. The height of a water vapor cloud is y m. The setup is symmetric to the y -axis, so we only need to simulate the first quadrant.

2.1. Field Equation

To construct the antenna power patterns, we begin with an electric field equation,

$$\overrightarrow{dE}(x, y) = \frac{E_0}{r} e^{-j\vec{k}\cdot\vec{r}} dl \hat{z} \quad (2)$$

to describe microwave propagation. Here dl stands for the length of the finite segments of the antenna along the x -axis, r is the distance from the center of the segment to one of the finite-size sources, \vec{k} is the wave vector and E_0 is the initial amplitude of the electric waves. The direction of the electric field is set up toward \hat{z} so that the strength of the electric field is simply the integral of $dE(x, y)$. The magnitude of the Poynting vector $|\overrightarrow{S_{av}}|$ is given by

$$|\overrightarrow{S_{av}}(x, y)| = \frac{1}{2\eta} \left| \int_{-\frac{D}{2}}^{\frac{D}{2}} d\vec{E} \right|^2, \quad (3)$$

where η is the intrinsic impedance of free space. D is the length of the array or the size of the parabolic antenna. The procedure to calculate the received power from a finite-size source is to solve $|\overrightarrow{S_{av}}|$ first, then integrate over the solid angle, Ω , to find $P_{ant}(\Omega)$, the total power transmitted by the source.

$$P_{ant}(\Omega) = \iint_{\Omega} \overrightarrow{S_{av}} \cdot d\vec{s} \quad (4)$$

where $d\vec{s}$ is an infinitesimal surface of the cloud.

2.2. Power patterns and Coordinate

Power patterns, also known as antenna patterns, are usually referred to the far-field power patterns (Balanis 1996). In the far-field region, the power patterns only depend on the direction so they generally are written down as normalized functions $P_n(\theta, \phi)$ in polar coordinates. However, in this memo the power patterns can be in either the near-field or far-field region. In the near-field region, it is better to illustrate the power patterns as functions of distance and direction. So we choose the Cartesian coordinate system in our figures.

2.3. Computational Method

Equation (2), (3) and (4) can not be processed directly by computers so we need to transform them first.

$$|\vec{S}_{av}| = \frac{1}{2\eta} \left| \sum_n \frac{e^{-j\vec{k} \cdot \vec{r}_{mn}}}{|\vec{r}_{mn}|} \right|^2 = \frac{1}{2\eta} \left[\left(\sum_n \frac{\cos(k \times r_{mn})}{r_{mn}} \right)^2 + \left(\sum_n \frac{\sin(k \times r_{mn})}{r_{mn}} \right)^2 \right] \quad (5)$$

is to calculate the magnitude of the Poynting vector at a position on the x - y plane. As shown in Figure 2, r or r_{mn} is the distance from an antenna segment n to a source m . The total number of the antenna segments is M , and the total number of the finite-size sources is N . To calculate the power transmitted by a cloud or a group of the finite-size sources to the antenna, the angles θ of \vec{r}_{mn} must be determined first, which at (x, y) is given by

$$\tan \theta(x, y) = \frac{\sum_n \frac{x_{mn}}{|\vec{r}_{mn}|^2}}{\sum_n \frac{y_{mn}}{|\vec{r}_{mn}|^2}}. \quad (6)$$

Finally,

$$P(y) = \sum_m^M |\vec{S}_{av}| \Delta x \times \pi y \cos \theta \quad (7)$$

gives the transmitting power of the cloud at the height of y to the antenna segments. To assure the simulation accuracy, the size of the antenna segments, Δl , must be less than one-tenth wave length, $\lambda/10$.

3. Simulation Result

3.1. Near-Field and Far-Field Patterns

The size of the antenna in our simulations, D , is 10 m, which is from -5 m to 5 m on the x -axis. The wavelength λ is 1 cm, approximately corresponding to the 22 GHz water line. Thus, the far-field limit in our simulations is $2D^2/\lambda$, 20 km (Balanis 1996). Below 20 km, the power patterns are in the near-field region, Fresnel zone; the power patterns beyond 20 km are in the far-field region, Fraunhofer zone, as shown in Figure 1.

In Figure 3 (a), at 200-m height, a Fresnel pattern is presented. In Figure 3 (b), the pattern particularly shows that the main lobe is smaller than the antenna dish size and the peaks appear at the edges of the main lobe. In Figure 3 (c) and Figure 3 (d), both of the far-field power patterns can be recognized. Comparing the power patterns at 20 km and 40 km, the peak power density reduces to half but the size of the main lobe doubles. This can be explained by the energy conservation. The power density decreases as the beam size increases.

By showing the line of the half maximum power density in Figure 4, we can clearly illustrate the antenna beam along the line of sight of the array. In the far-field region, the antenna beam looks like a cone with a solid angle depending on the antenna size; however, in the near-field region, the antenna beam lacks a simple geometric shape.

3.2. The Impact of Finite-size Clouds of Water Vapor

The brightness temperatures of infinite-size water vapor clouds are the same as the antenna temperatures regardless of their heights. Additionally, according to the ATM simulations (Staguhn et al. 1998), the cloud altitude barely affect the 22 GHz water line. Therefore, for a 22 GHz WVR system, we can derive the path delays without knowing the heights of water vapor clouds. However, with finite-size clouds, the cloud height and size affect the antenna temperature enormously. Based on Figure 3 (c) and (d), comparing a 20-m wide cloud at 20-km height and a 20-m wide cloud at 40-km height with the same temperature, the detected power from the latter is only half of the former. Therefore, the antenna temperature may fail to respond to path delay change accordingly. We note that this is not equivalent to the beam filling factor, which decreases much faster.

To further investigate the effect of finite-size water vapor clouds, we compare the brightness temperature and its corresponding antenna temperature with different-size clouds at different heights. Here, we define the detection efficiency as the ratio of antenna temperature to brightness temperature. In Figure 5, we show the detection efficiencies in different cases. For example, a 10-m cloud, the antenna temperature reduces to only 90% at 1 km and 80% at 5 km. A 20-m cloud's antenna temperature is reduced by 5% of its brightness temperature at 5 km. Generally, the larger cloud has the higher detection efficiency.

4. Conclusions

We have demonstrated the antenna patterns in the near- and the far-field regions. The beam size can be either larger or smaller than the parabolic antenna size and the peaks of the power patterns are not necessarily at the centers. The detection efficiency varies widely depending on the sizes and heights of water vapor clouds. As a result, the scale factor of the 22 GHz water line is no longer a constant and varies under real weather conditions. Although theoretically the cloud height play a minor role in the WVR phase correction scheme. Our simulations show that, with small water vapor clouds, the antenna temperature still can suffer from the dependence on the cloud size and height.

Since WVRs have low detection efficiency with small water vapor clouds, a higher scale factor will be expected. Practically all of clouds are finite-size so that the antenna temperature is smaller than the brightness temperature, i.e. the scale factor should often is higher. However, the scale factor can be negative occasionally when a significant amount of water vapor is located in the main beam but not in the column. Our simulations suggest that atmospheric models (Stirling et al. 2005; Pardo et al. 2001) should include small-size water vapor clouds to improve the performance of the WVR phase correction.

REFERENCES

- Balanis, C. A., "Antenna Theory Analysis and Design", 2nd, Wiley, 1996.
- Chandler, C. J., Brisken, W. F., Butler B. J., Hayward, R. H. and Willoughby, B. E. "RESULTS OF WATER VAPOUR RADIOMETRY TESTS AT THE VLA", EVLA MEMO 73, 2004.
- Hills, R. and Richer, J., "Water Vapour Radiometers for ALMA", ALMA Memo 303, 2000.
- Marvel, K. B. and Woody, D. P., "Phase correction at millimeter wavelengths using observations of water vapor at 22 GHz", Proc. SPIE, 3357, 442-452, 1998.
- Pardo, J. R., Cernicharo, J. and Serabyn, E., "Atmospheric Transmission at Microwaves (ATM): An Improved Model for mm/submm applications", IEEE Trans. on Antennas and Propagation, 2001.
- Staguhn, J., Harris, A. I., Plambeck, R. L. and Welch, W. J., "Phase correction for the BIMA array: atmospherical model calculations for the design of a prototype correlation radiometer", BIMA Memo 67, 1998.
- Stirling, A., Richer, J. Hills, R. and Lock, A., "Turbulence simulations of dry and wet phase fluctuations at Chajnantor", ALMA Memo 517, 2005.
- Thompson, R., Moran, J. and Swenson, G., " Interferometry and Synthesis in Radio Astronomy Interferometry and Synthesis in Radio Astronomy", Wiley-Interscience, 2001.
- Waters, J. W., "Methods of experimental physics: Astrophysics Part B: Radio Telescopes", Academic Press, 122-176, 1976.

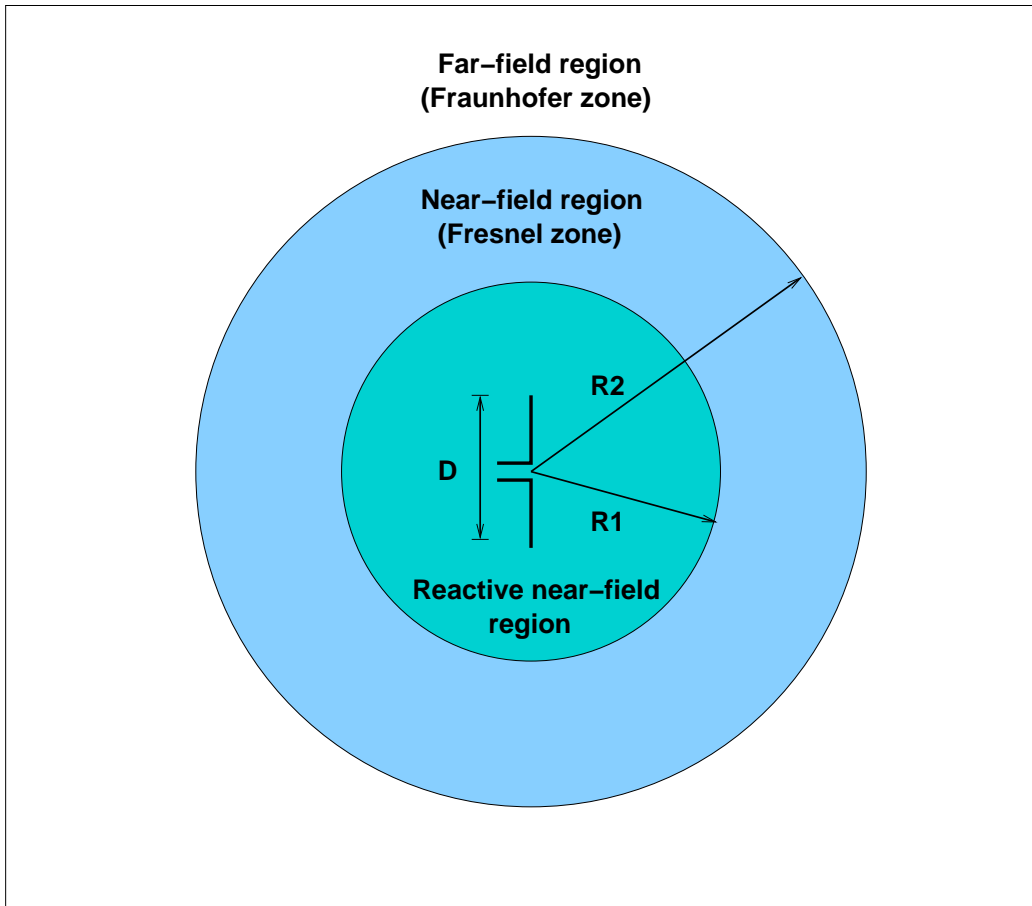


Fig. 1.— Antenna field including the far-, near- and reactive near-fields. $R_1 = \sqrt{D}/\lambda$ and $R_2 = 2D^2/\lambda$. D is the size of the antenna, 10 m, and λ , 1 cm, is the wave-length. Thus, R_1 is 200 m and R_2 is 20 km.

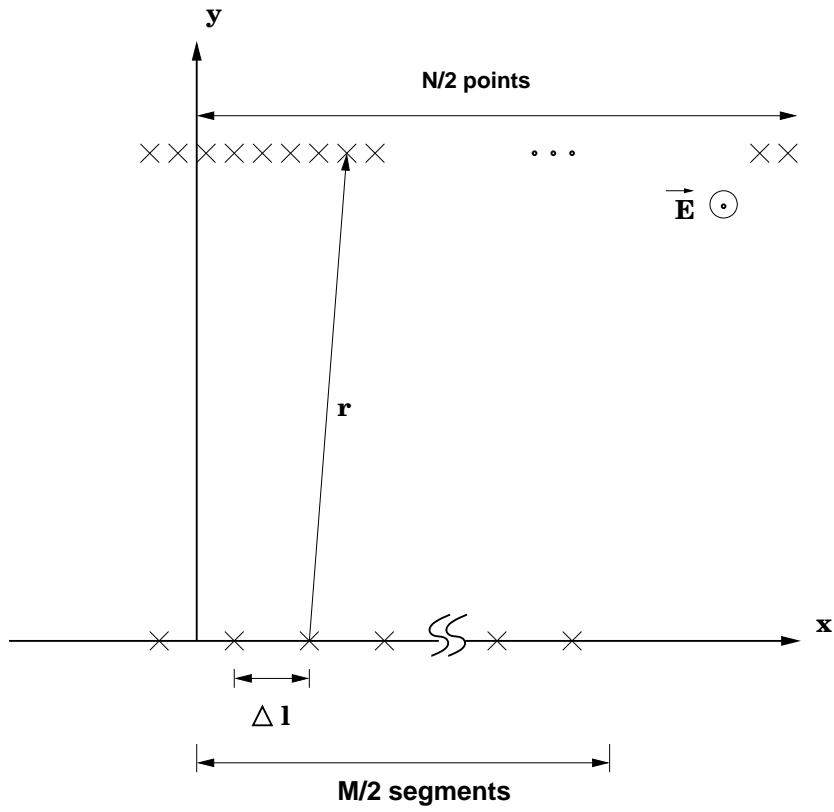


Fig. 2.— Simulation setup. The number of the antenna segments is M , the number of the sample points on each layer is N , r is the distance from an antenna segment to a source, and dl is the length of the antenna segments.

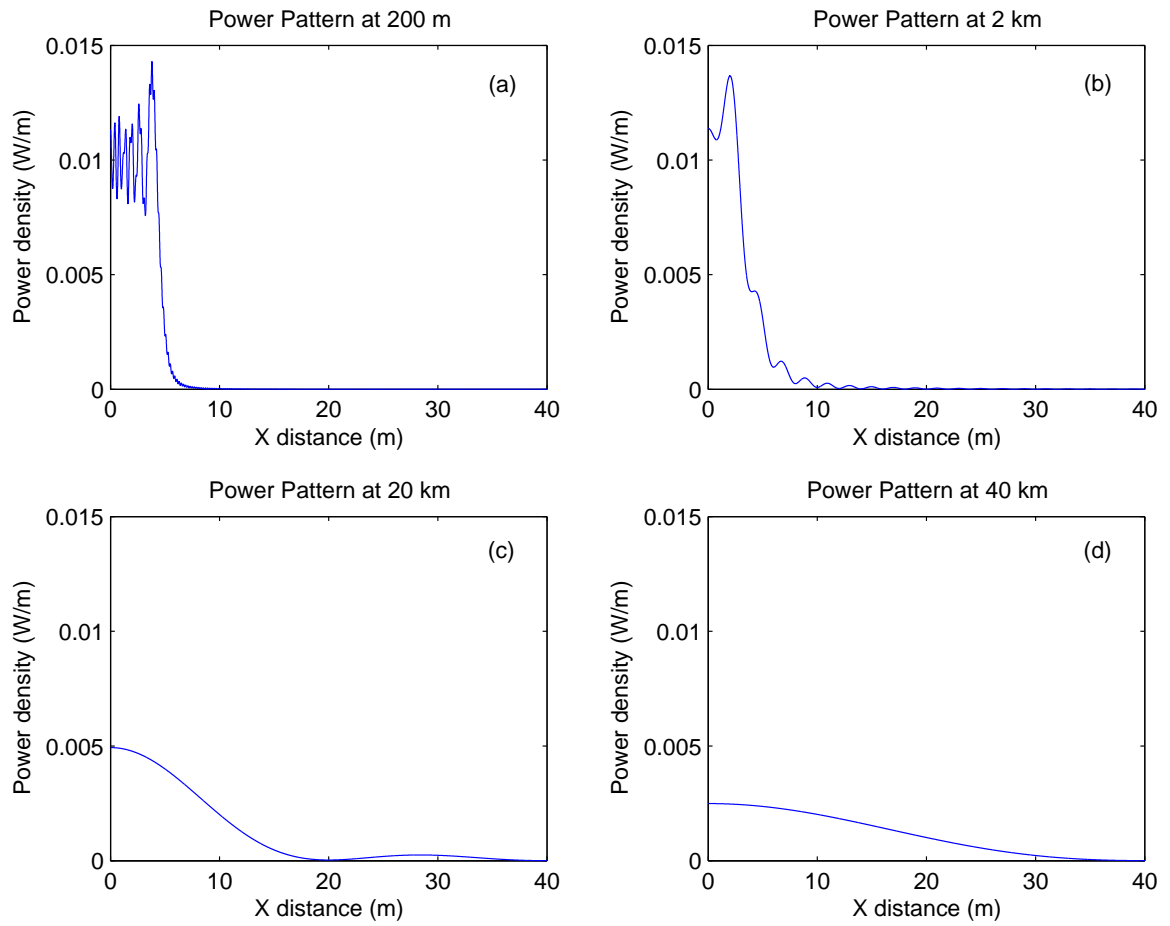


Fig. 3.— Four power patterns at 200 m (a), 2 km (b), 20 km (c) and 40 km (d) are shown respectively.

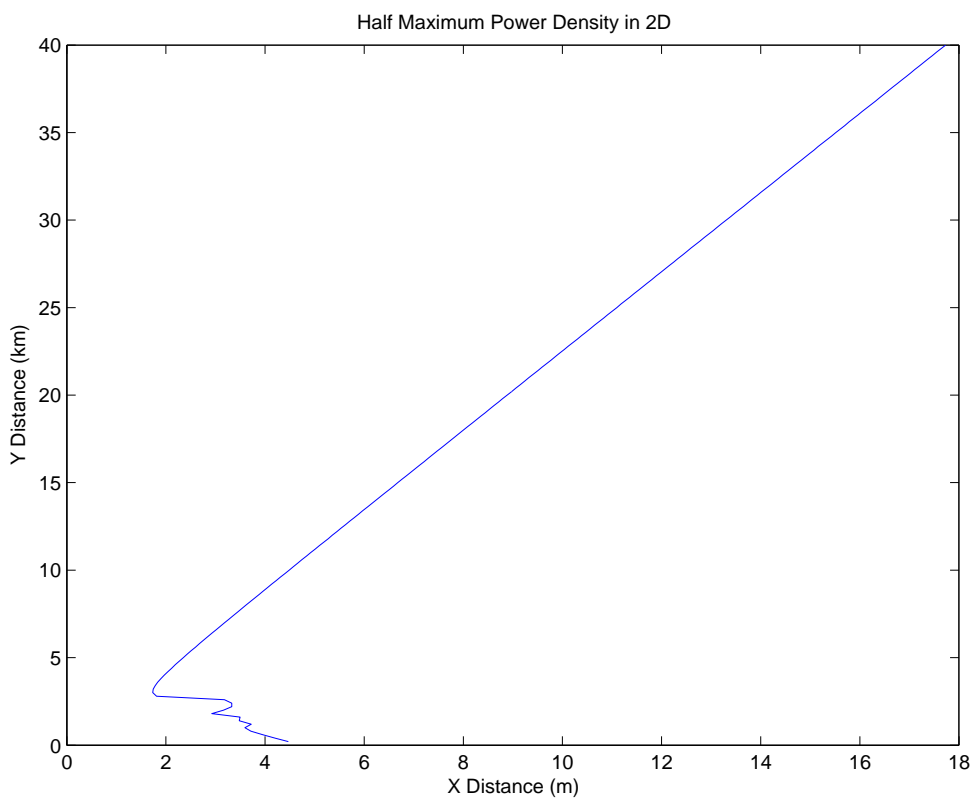


Fig. 4.— The simulated beam size. The antenna is located from -5 m to 5 m along the x -axis. The straight portion of the line implies far-field patterns; the curvy portion below 4-km height on the y -axis indicates the irregular near-field patterns.

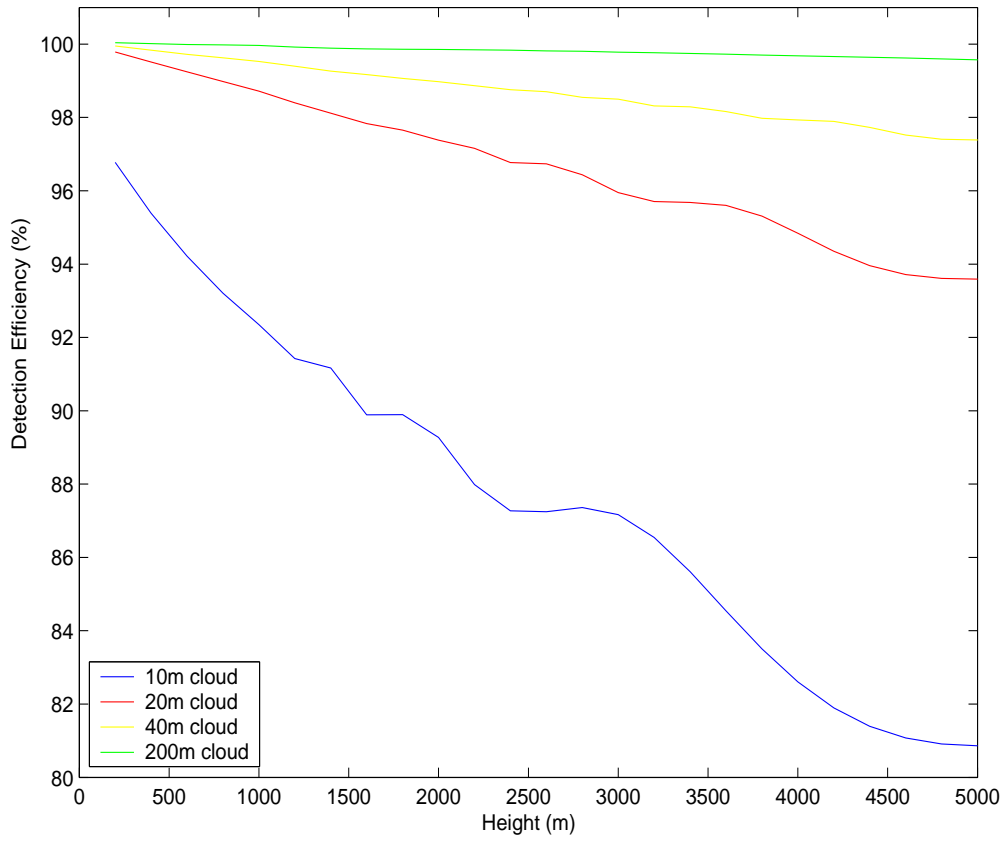


Fig. 5.— Detection efficiency. The detection efficiency is defined as the ratio of the antenna temperature to the sky brightness temperature.